

Fission barriers and fission paths of the ^{70}Se nucleus within a microscopic approach

L. Bonneau¹ and P. Quentin^{1,2}¹*Los Alamos National Laboratory, Theoretical Division, MS B283, Los Alamos, New Mexico 87545, USA*²*Centre d'Etudes Nucléaires de Bordeaux-Gradignan, CNRS-IN2P3 and Université Bordeaux-I, BP 120, F-33175 Gradignan, France*

(Received 27 January 2005; published 22 July 2005)

The fission barriers as well as different fission paths of the ^{70}Se nucleus have been microscopically investigated within a constrained Skyrme-Hartree-Fock plus BCS approach using the SkM* effective interaction. The effects of intrinsic reflection asymmetric deformations have been taken into account while axial symmetry around the fission direction has been assumed. The two-body part of the center of mass correction has been included in a perturbative way and has been found to weakly contribute to the calculated barrier heights. Upper limits of the latter have been evaluated as the heights with respect to the ground state energy of the lowest saddle points obtained along continuous paths in a reasonably dimensioned collective space connecting one-body shaped and two-body shaped configurations. They have been found somewhat higher than what is expected from other theoretical studies.

DOI: 10.1103/PhysRevC.72.014311

PACS number(s): 21.60.Jz, 24.75.+i

I. INTRODUCTION

In a previous work [1] extensive calculations of fission barriers in heavy nuclei have been performed within the Skyrme-Hartree-Fock mean field approximation including pairing correlations in the BCS approximation. Since this approach has been proven to satisfactorily describe the considered fission barrier heights, we have found it interesting to extend such a study to the completely different region of light nuclei, specifically here the ^{70}Se isotope. As well known (see, e.g., Ref. [2]), when the fissility parameter x decreases, the saddle point shape becomes more and more necked in, or in other words the scission point becomes closer to the saddle point. Below the so-called Businaro-Gallone x -value, one even finds that only conditional liquid drop fission barriers exist for given fragmentations. The ^{70}Se nucleus having a fissility parameter $x = 0.33$ (with $(Z^2/A)_{\text{crit}} = 50.13$ [3]) does qualify *a priori* for such an instability at the saddle point with respect to reflexion asymmetric deformations. Moreover it has been argued from semiclassical calculations (see [4]) that the large value of the curvature coefficient associated in such a model approach with Skyrme effective forces should yield fission barriers in light nuclei much too high. Assessing the value of our approach in such a nuclear region is thus the main motivation for the present study. Our choice of a particular light nucleus has been naturally oriented towards the ^{70}Se isotope since recent experimental data [5] are available and some calculations have been already performed for that nucleus [6,7].

II. THEORETICAL FRAMEWORK AND CALCULATION PROCEDURE

As in Ref. [1] the Skyrme effective force, in its SkM* parametrization [8], has been used. As is well known, it has rather good surface properties which makes it well suited for the description of very elongated nuclear shapes as encountered during the fission process.

The usual BCS formalism with a seniority force has been implemented to treat the pairing correlations. The constant matrix elements of the seniority force are given for the q -charge state by $G_q = g_q/(11 + N_q)$ in MeV where N_q is the number of particles of charge q , $g_n = 17.1$ MeV and $g_p = 16.5$ MeV. This parametrization has been taken from the calculations of Ref. [9] dealing with the spectroscopic properties of nuclei in the same region. The single particle states entering the BCS equations are contained in the range $]-\infty, \lambda + 5]$ in MeV (where λ is the chemical potential) and their contribution is weighted at the edges by a Fermi factor whose diffuseness parameter has the value of 0.2 MeV. In all the calculations presented here we have allowed for left-right asymmetrical deformations, measured by the expectation value of the axial octupole moment $\langle \hat{Q}_{30} \rangle$ given, in spherical coordinates by

$$\langle \hat{Q}_{30} \rangle = \int d\mathbf{r} \rho(\mathbf{r}) r^3 Y_3^0(\theta, \phi), \quad (1)$$

[in what follows $\rho(\mathbf{r})$ represents the mass, i.e., neutron plus proton, distribution]. When the left-right symmetry is broken, we have further assumed the axial symmetry along the z -axis. When the left-right symmetry is imposed or borne out by the potential energy surface, in some instances we have relaxed the former axial symmetry. Both axial and nonaxial quadrupole deformations are defined by the expectation values $\langle \hat{Q}_{20} \rangle$ and $\langle \hat{Q}_{22} \rangle$ through

$$\langle \hat{Q}_{20} \rangle = \int d\mathbf{r} \rho(\mathbf{r}) (3z^2 - r^2) \quad (2)$$

$$\langle \hat{Q}_{22} \rangle = \int d\mathbf{r} \rho(\mathbf{r}) (x^2 - y^2), \quad (3)$$

and for small deformations, they can be expressed in terms of the Bohr parameters β and γ [10] at first order in β as follows:

$$\langle \hat{Q}_{20} \rangle = \sqrt{\frac{5}{\pi}} A \langle r^2 \rangle \beta \cos \gamma, \quad (4)$$

$$\langle \hat{Q}_{22} \rangle = \sqrt{\frac{5}{3\pi}} A \langle r^2 \rangle \beta \sin \gamma, \quad (5)$$

where $\langle r^2 \rangle$ is the averaged expectation value of the squared radius:

$$\langle r^2 \rangle = \frac{1}{A} \int d\mathbf{r} \rho(\mathbf{r}) r^2. \quad (6)$$

The inverse relations are therefore (at first order in β):

$$\beta = \sqrt{\frac{\pi}{5}} \frac{\sqrt{\langle \hat{Q}_{20} \rangle^2 + 3 \langle \hat{Q}_{22} \rangle^2}}{A \langle r^2 \rangle}, \quad (7)$$

$$\tan \gamma = \frac{\sqrt{3} \langle \hat{Q}_{22} \rangle}{\langle \hat{Q}_{20} \rangle}. \quad (8)$$

Since our code gives rise to calculations with a basis rather close to axial symmetry having O_z as a symmetry axis, the relevant ranges for γ are on the prolate and oblate sides, respectively:

$$0 \leq \gamma \leq \frac{\pi}{6} \quad (\text{case 1}), \quad (9)$$

$$\pi \leq \gamma \leq \frac{7\pi}{6} \quad (\text{case 2}) \quad (10)$$

β being always positive. Correspondingly, the axial and nonaxial quadrupole moments $\langle \hat{Q}_{20} \rangle$ and $\langle \hat{Q}_{22} \rangle$ are both, respectively, positive and negative in the two above cases. Nevertheless the γ' -values traditionally displayed on figures (see, e.g., our Fig. 2 where we have kept the notation γ) are defined by

$$\gamma' = \gamma \quad (\text{case 1}), \quad (11)$$

$$\gamma' = -\gamma + \frac{4\pi}{3} \quad (\text{case 2}), \quad (12)$$

such that they range between 0 and $\pi/3$. Moreover one can note that, in our code, x and y are interchangeable by construction so that the sign of $\langle \hat{Q}_{22} \rangle$ when constraining this moment is irrelevant.

In order to calculate the fission barrier height, we have first to determine the most relevant fission paths from the ground state to scission configurations and beyond, with a particular attention paid to the saddle points. In that respect we have to find paths along which all the moments of the nuclear density remain continuous functions of the elongation parameter chosen here to be represented by the mass quadrupole moment $\langle \hat{Q}_{20} \rangle$. The barrier height is thus the energy of the lowest saddle point relative to the ground state.

To better understand the transition between the one-body shaped solutions around the “exit point” (defined in Sec. III B) and those in the fission fragment valleys, one has to evaluate the thickness of the “neck” of matter appearing between nascent fragments. One possible way to do so is to compute the hexadecapole moment in spherical coordinates by

$$\langle \hat{Q}_{40} \rangle = \int d\mathbf{r} \rho(\mathbf{r}) r^4 Y_4^0(\theta, \phi). \quad (13)$$

One can alternatively make use of another global variable previously introduced by Berger *et al.* [11]:

$$\langle \hat{Q}_N \rangle = \int d\mathbf{r} \rho(\mathbf{r}) e^{-(z-z_{\min})^2/a^2}. \quad (14)$$

The width of the Gaussian a is chosen to be of the order of the nucleon–nucleon interaction range ($a = 1$ fm here) and its

center z_{\min} is defined as the point on the fission axis where the nuclear density reaches its lowest value between both (nascent) fragments. For a two-body shaped system, $\langle \hat{Q}_N \rangle$ is vanishing when the tip-distance between the soft edges is much larger than the a parameter. On the contrary, a one-body shaped nucleus has a finite expectation value $\langle \hat{Q}_N \rangle$ which depends on the compact character of the nucleus, mainly determined by its elongation ($\langle \hat{Q}_{20} \rangle$ -value).

Since the pioneering work of Swiatecki [12], followed by the microscopic-macroscopic calculations of Pashkevich [13–16] and Möller [17–19] as well as the microscopic HFB calculations of Berger and collaborators [11,20,21] and some others [22–25], one knows that the potential energy landscape describing the descent from saddle points to scission points is rather complicated. Quite a number of collective variables appear necessary to describe properly the minimal topology able to reproduce some experimental data (as, e.g., the transition between and/or the coexistence of symmetrical and asymmetrical components in the fragments mass yields [26–29]). It is therefore of paramount importance to be able to probe the energetic response of the nuclear system to various deformation modes. In view of the enormous numerical effort to exhaustively map the energy on a mesh of all relevant collective variables [30], it is of practical interest in microscopic calculations to perform cuts according to various supplemental conditions like constraining one (or more) collective variable to have a given value. This has been very well illustrated in the seminal work of Berger and collaborators [11,20,21] where the various relevant variables and topologies have been sorted out.

To achieve this goal, in practice, one has to make sure that solving the constrained variational problem one guarantees with a sufficient accuracy that the requested condition(s) is (are) met. Following techniques originated in this context by the Bruyères-le-Châtel group [31], we have developed, only in the axially symmetric case, an algorithm which adjusts iteratively the Lagrange multipliers λ_i to provide the requested expectation values of the constraint operators \hat{Q}_i . This has been done in close collaboration with Dr. Samsœn (CENBG Bordeaux). The idea consists of calculating the relevant $\delta\lambda_i$ values from the differences $\delta\langle \hat{Q}_j \rangle$ between the computed and expected values at the first order of perturbation theory. This implies the inversion of a matrix similar to the inertia matrix in the Inglis cranking approximation.

In our codes, the single-particle HF wave functions have been expanded onto the axially deformed harmonic oscillator basis which has obviously to be truncated in practice. This introduces, as is well known, spurious dependence upon the basis parameters that has been carefully checked as outlined in Ref. [1]. Namely we have optimized the basis parameters all along the curve from the ground state to the exit point at $\langle \hat{Q}_{20} \rangle \approx 44$ barns (b) and along the two fusion valleys displayed in Fig. 3 (see next section for explanations). All the results reported in this paper have been obtained with the basis size parameter $N_0 = 12$ (with the notation of Ref. [1]).

Our calculations as is well known, deal with solutions in the intrinsic frame. Two types of approximate corrections are considered here to tentatively cure the symmetry breaking inherent to this situation. They concern the rotational and

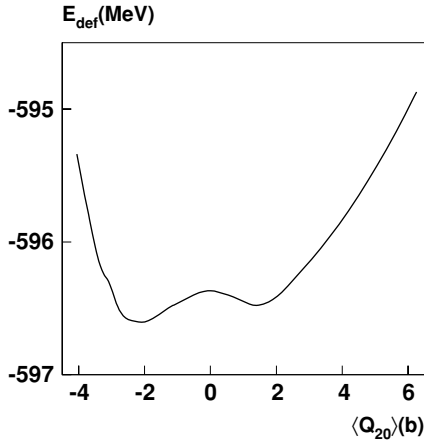


FIG. 1. Deformation energy curve of ^{70}Se around the spherical point.

translational invariances. Some consequences of these approximations (presented at length in various other places, see, e.g. [1]) will be discussed below, particularly in Sec. IV.

III. RESULTS: FISSION PATHS AND BARRIER HEIGHTS

We first report on the results concerning the potential energy surface. They aim at finding out the lowest relevant paths from the ground state to some final states in which fragments are well separated.

A. Around the ground state deformation

To find the lowest minimum, i.e., the ground state, we have initiated the constrained Hartree-Fock iterative process with a spherical Woods-Saxon single-particle potential and a constraint on the elongation $\langle \hat{Q}_{20} \rangle$ released after a few iterations. This initial constraint acts as a perturbation taking the nucleus away from the spherical shape and, once released, enables us to find local minima in the vicinity of the spherical point (this point being itself possibly included). Restricting ourselves first to axially symmetrical shapes, we have obtained two almost degenerate minima, namely one oblate at $\langle \hat{Q}_{20} \rangle \approx -2.2$ b and one prolate at $\langle \hat{Q}_{20} \rangle \approx 1.5$ b. The latter is found to be about 150 keV higher than the oblate one while the spherical barrier, from the prolate minimum to the spherical point, is even smaller (see Fig. 1).

Using the expressions (4) and (5) the corresponding β -values are, respectively, $\beta \approx 0.15$ (oblate) and $\beta \approx 0.10$ (prolate). *A posteriori* we see that these values are reasonably small as to allow to truncate the expansion of $\langle \hat{Q}_{20} \rangle$ and $\langle \hat{Q}_{22} \rangle$ at first order in β .

Actually the imposition of axial symmetry leads, in that case, to rather deceptive conclusions. As shown in Fig. 2 where various cuts of the potential energy surface in the (β, γ) usual sextant are shown, this nucleus is essentially a spherical oscillator, on which a rather shallow gutter running from $\beta \approx 0.10$ on the prolate side to $\beta \approx 0.15$ on the oblate side is to be noted. It is worth noting that this feature is at variance with those underlying some other theoretical approaches (see

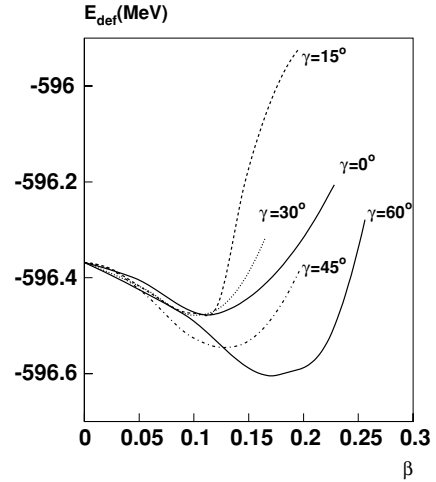


FIG. 2. Cuts in the (β, γ) plane (note the very dilated scale of the energy).

Refs. [32–34]) emphasizing an alleged prolate-oblate coexistence for this nucleus. The experimental spectrum (see, e.g., Fig. 3 of Ref. [34]) does not allow us to confirm either theoretical finding. One finds a rather nice vibrational pattern for the sequence of first 0^+ , 2^+ , 4^+ states [energy and $B(E2)$ ratios close to 2]. However quasi- β and quasi- γ band structure might be present as well. Nevertheless, it is quite clear that the consideration of any structure of the mass parameters in conjunction with our rather flat energy surface might stabilize the collective solution in a smaller deformation range. This would be more consistent with the data. In this context, it is interesting to note that, as it will be discussed later, including the two-body part of the center of mass correction produces also a perturbation of our potential energy surface yielding a statically preferred prolate equilibrium shape.

B. “Ground state” ascending valley

At first, we discuss what we call the “ground state” ascending valley (i.e., ascending upon increasing the \hat{Q}_{20} operator expectation value). To describe this valley, we have started from the prolate equilibrium (for purely axial shapes) solution generating step by step self-consistent solutions whose mass quadrupole moments differ by about 5 b on average. In doing this, we allowed for a possible left-right reflection (mirror) asymmetry but not for a violation of the axial symmetry. As seen in Fig. 3, we have obtained a potential energy curve monotonically increasing by about 50 MeV when going from $\langle \hat{Q}_{20} \rangle = 1.5$ b to $\langle \hat{Q}_{20} \rangle \approx 44$ b.

A necessary condition for considering the ensemble of such solutions as forming a valley is that a collection of expectation values of relevant collective operators appears to be smoothly varying as function of the constrained quantity—here $\langle \hat{Q}_{20} \rangle$. Of course, this is not a sufficient condition since one cannot guarantee that the expectation value of some operator not looked at in the present calculations would not exhibit wild excursions out of a smooth path. This remark is valid for all calculations of this type (along some cut in the collective space as here or building up a mesh in a potential energy

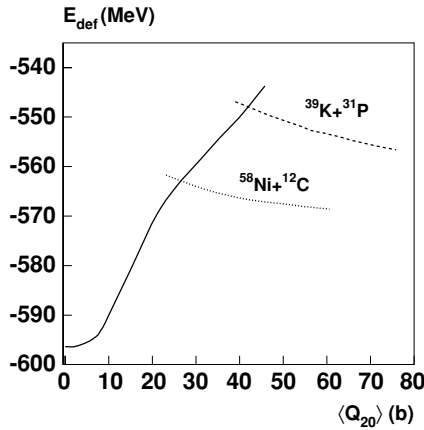


FIG. 3. Deformation energy curves of ^{70}Se obtained in the conditions described in the text. The full line is the ground state ascending valley (one-body shapes) whereas the discontinuous lines denote two-body shapes: the dashed line corresponds to the $^{39}\text{K} + ^{31}\text{P}$ fragmentation, whereas the dotted one corresponds to the $^{58}\text{Ni} + ^{12}\text{C}$ fragmentation.

surface necessarily restricted to a limited number of collective variables as, e.g., in Ref. [30]).

At least, one should make sure that the supposedly most important modes are reasonably well described by the retained operators. In our case, we have chosen three such operators, one related to the mass asymmetry, namely \hat{Q}_{30} , and the two others related to the neck-formation modes \hat{Q}_{40} and \hat{Q}_N . Obviously the choice of these operators is not without problems, beyond the mere consideration of the limited number of studied modes. Indeed, they neither are independent collective variables nor unambiguously define a physical configuration. By the latter, we do not mean that they are not univocally defined in a mathematical sense (see the above discussion), but rather that they cannot define in a pertinent way the whole span of shapes going from one single spherical (or quasispherical for that matter) nucleus to two separated deformed fragments. The hexadecapole moment is of poor usefulness in the latter case while $\langle \hat{Q}_N \rangle$ is hardly meaningful in the former case. This is precisely why we have decided to consider systematically both. The expectation values of \hat{Q}_{30} , \hat{Q}_{40} , and \hat{Q}_N along the ground state ascending valley are displayed in Fig. 4. They all show, up to small kinks (consistently in the $\langle \hat{Q}_{40} \rangle$ and $\langle \hat{Q}_N \rangle$ curves) near $\langle \hat{Q}_{20} \rangle = 12$ b, rather smooth behaviors. The corresponding sequence of shapes is displayed in Fig. 5. It is worth noting that we have found around $\langle \hat{Q}_{20} \rangle = 21$ b some octupole instability, as illustrated in Fig. 6.

Upon increasing the deformation from $\langle \hat{Q}_{20} \rangle = 15$ b for instance, one experiences the apparition of a shallow valley in the direction of increasing $\langle \hat{Q}_{30} \rangle$ values near $\langle \hat{Q}_{20} \rangle = 21$ b. This pattern transforms itself in a shouldering of lesser and lesser importance at higher and higher $\langle \hat{Q}_{20} \rangle$ values, to almost disappear near $\langle \hat{Q}_{20} \rangle \approx 30$ b. It is important to note that we have found no evidence of a smooth connection between this octupole instability region and the second descending valley which will be discussed below and whose energy curve as a function of $\langle \hat{Q}_{20} \rangle$ crosses the energy curve of the presently

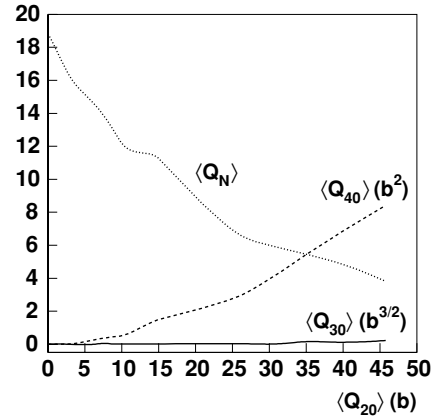


FIG. 4. Variation of the axial octupole, hexadecapole, and “neck” moments as functions of the elongation $\langle \hat{Q}_{20} \rangle$ along the ground state ascending valley (see text for definition).

studied ascending ground state valley at almost the same quadrupole deformation—namely $\langle \hat{Q}_{20} \rangle = 26.5$ b.

At $\langle \hat{Q}_{20} \rangle \approx 44$ b, which corresponds to the so-called “exit point,” the ground state ascending valley terminates, as will be discussed in the next subsection. This means, in practice, that at such quadrupole moment values and at larger ones, we did not find any stable symmetrical equilibrium solutions whose collective moment values would be smoothly connected with those obtained at lesser elongations.

As mentioned above, we have assumed axially symmetric shapes all along the different studied paths. This has been tested in one point belonging to the ground state ascending valley by making a cut in the $\langle \hat{Q}_{22} \rangle$ direction. More precisely, slightly before (upon deforming away from the ground state) the intersection point of the ground state ascending path and the lowest descending valley (discussed in Sec. III D below), that is at $\langle \hat{Q}_{20} \rangle = 26$ b, we have checked that our axial solution ($\langle \hat{Q}_{22} \rangle = 0$, thus $\gamma = 0$) is stable against triaxial deformations (see Fig. 7). In terms of the (β, γ) parameters, it corresponds to a section in the γ direction from 0° to 4° at a fixed β -value, namely $\beta = 1.1$.

C. Around the exit point

When approaching $\langle \hat{Q}_{20} \rangle$ -values of the order of 40 b, the symmetrical solution¹ corresponding to the ground state ascending valley becomes less and less stable against deformations narrowing the neck region ($\langle \hat{Q}_N \rangle$ deformations). This can be seen in Fig. 8 where the deformation energy has been plotted as a function of the expectation value of the neck operator \hat{Q}_N for different fixed $\langle \hat{Q}_{20} \rangle$ -values from 38 to 50 b.

These sections of the potential energy surface in the $\langle \hat{Q}_N \rangle$ direction have been obtained in the following way. At a given $\langle \hat{Q}_{20} \rangle$ -value, we have started from the $\langle \hat{Q}_N \rangle$ -value (typically between 4 and 5) associated with the solution in the so-called ground state ascending valley (which has been found to be

¹In what follows, “symmetrical” or “asymmetrical” will refer to the left-right reflexion symmetry.

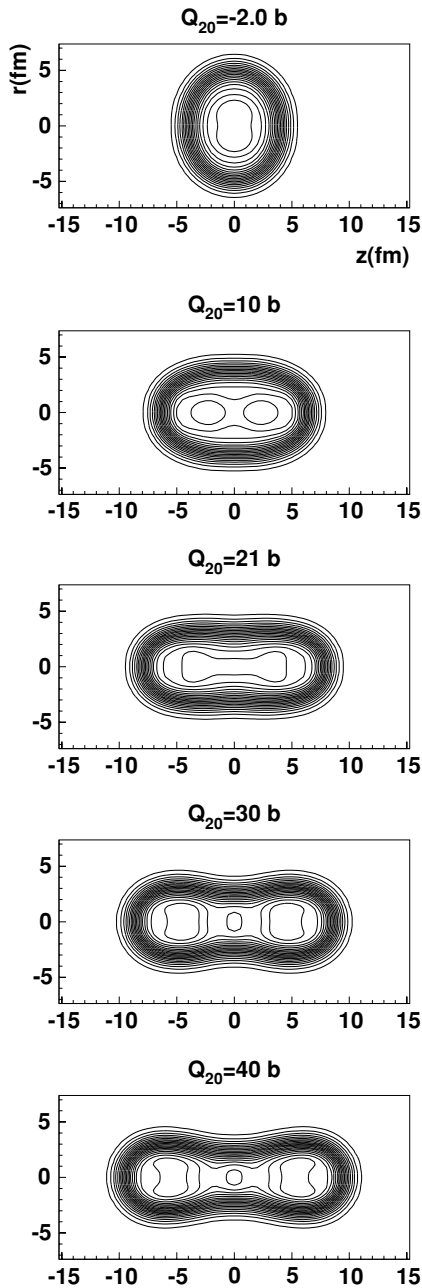


FIG. 5. Nuclear density contours at different $\langle \hat{Q}_{20} \rangle$ -values along the ground state ascending valley.

symmetrical, see Fig. 6). Then, we have varied the constraint on $\langle \hat{Q}_N \rangle$ for both larger and smaller values so as to describe the corresponding deformation energy curve. This leads to the full lines in Fig. 8. It appears that the (symmetrical) solution lying in the ground state ascending valley and corresponding to the minimum around $\langle \hat{Q}_N \rangle = 5$ of the $\langle \hat{Q}_N \rangle$ -sections is stable for $\langle \hat{Q}_{20} \rangle$ -values lower than or equal to 44 b. This minimum becomes less and less pronounced when increasing $\langle \hat{Q}_{20} \rangle$ and tends to disappear around 44 b, where it ends up by exhibiting a very shallow pattern, close to a mere “shoulder.” That is precisely what characterizes an exit point, referred to as the “symmetrical exit point” in the following since the corresponding octupole moment is equal to zero.

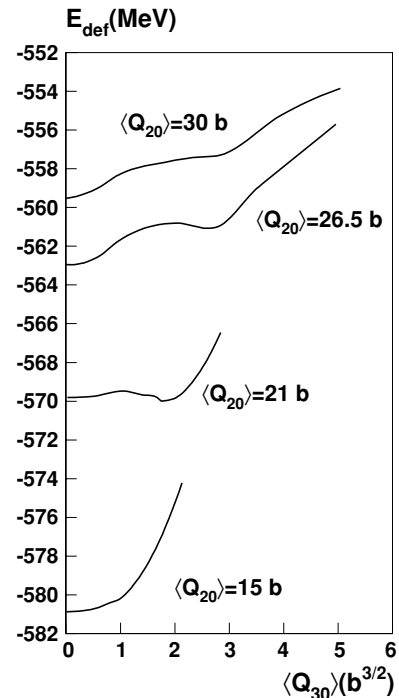


FIG. 6. Sections in the $\langle \hat{Q}_{30} \rangle$ direction for four $\langle \hat{Q}_{20} \rangle$ -values around the octupole instability observed at $\langle \hat{Q}_{20} \rangle \approx 21$ b along the ground state ascending valley.

At very low—close to zero— $\langle \hat{Q}_N \rangle$ -values, a second minimum develops in the curves of Fig. 8 starting from $\langle \hat{Q}_{20} \rangle \approx 39$ b upon increasing the elongation. The corresponding solution is two-body shaped and slightly asymmetric. At all elongations considered here it corresponds to the $^{39}\text{K}+^{31}\text{P}$ fragmentation. The set of such minima at various elongations forms what is called here the $^{39}\text{K}+^{31}\text{P}$ descending valley (dashed line of Fig. 3) and will be discussed in greater details in the Sec. III D. Such a coexistence at a given $\langle \hat{Q}_{20} \rangle$ -value of ascending and descending valleys, generally separated by a ridge, has already been found in similar calculations (see,

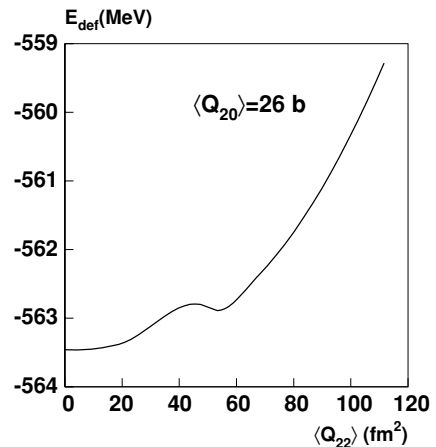


FIG. 7. Section of the potential energy surface at $\langle \hat{Q}_{20} \rangle = 26$ b in the $\langle \hat{Q}_{22} \rangle$ direction.

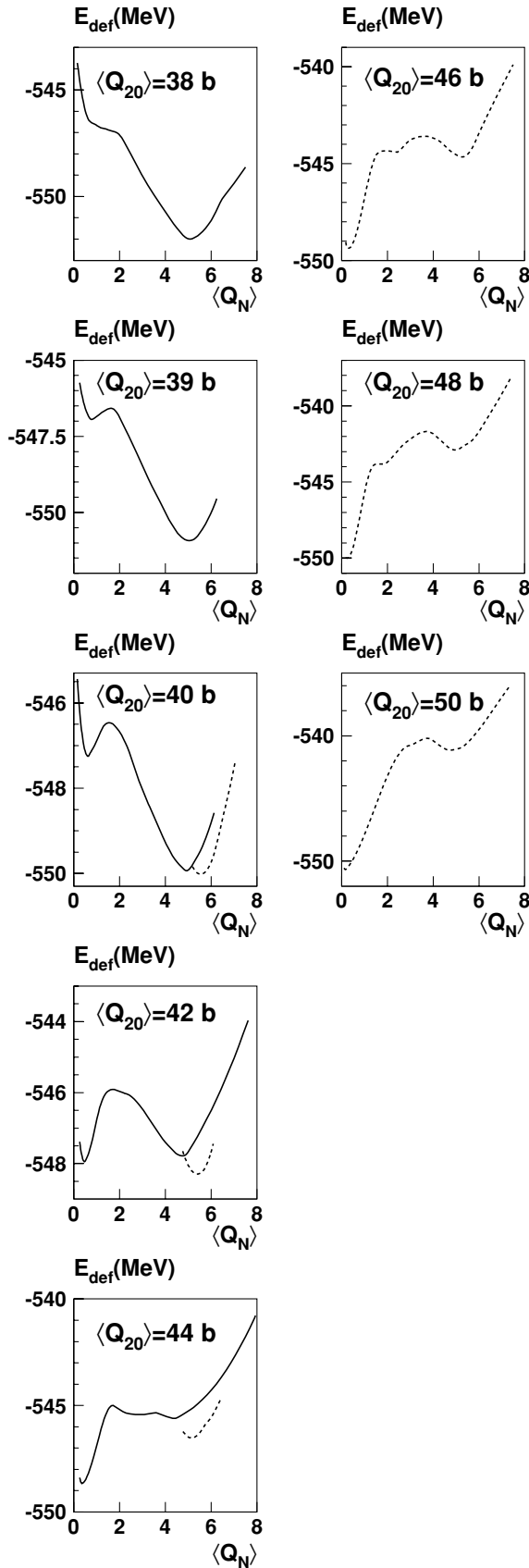


FIG. 8. Sections in the $\langle \hat{Q}_N \rangle$ direction at various $\langle \hat{Q}_{20} \rangle$ -values around the exit point.

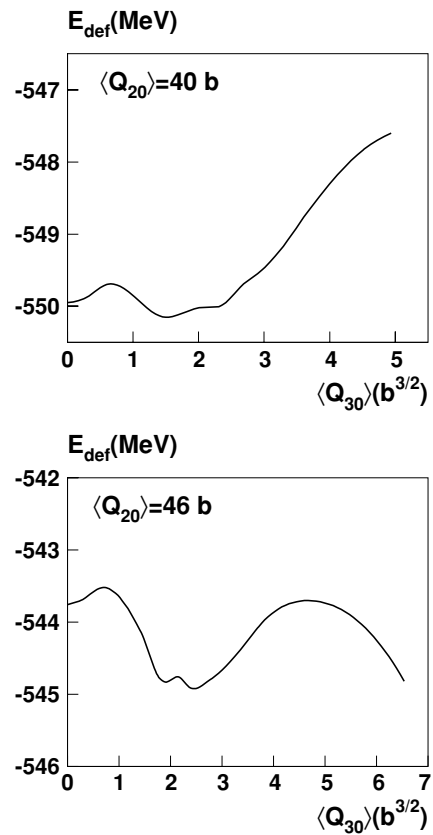


FIG. 9. Sections in the $\langle \hat{Q}_{30} \rangle$ direction at $\langle \hat{Q}_{20} \rangle = 40$ b and $\langle \hat{Q}_{20} \rangle = 46$ b.

e.g., Ref. [11] and the Figs. 2–4 of Ref. [22]). One can also remark that the minima associated with the one-body shaped solution (corresponding to the ground state ascending valley) and the above two-body shaped solution coexist for elongations contained between $\langle \hat{Q}_{20} \rangle = 39$ b and $\langle \hat{Q}_{20} \rangle = 44$ b, and that, for $\langle \hat{Q}_{20} \rangle = 42$ b, they have approximately the same energy. Figure 8 displays a very typical pattern of shape transition in an isotopic series (observed long ago in calculations of shape coexistence/transition in deformed nuclei). It has been first illustrated in the context of fission/fusion of two nuclei, see Fig. 3 of Ref. [11].

In addition, as it can be seen, e.g., in Fig. 9, displaying the deformation energy as a function of the expectation value of \hat{Q}_{30} at two different fixed $\langle \hat{Q}_{20} \rangle$ -values—namely 40 b and 46 b—an asymmetrical solution has also been found. Then we have made a cut in the $\langle \hat{Q}_N \rangle$ direction at the same elongations as above mentioned but starting from this asymmetrical solution. We have thus obtained the dashed curves of Fig. 8. It is interesting to notice that, whereas the symmetrical ground state ascending valley ends around $\langle \hat{Q}_{20} \rangle = 44$ b, the asymmetrical solution remains stable against neck deformations up to $\langle \hat{Q}_{20} \rangle = 50$ b at least, where the minimum is still rather well pronounced (being approximately 1 MeV deep).

All along the above-discussed sections of the energy surface in the $\langle \hat{Q}_N \rangle$ direction, it has been checked that the (axial) octupole and hexadecapole moments corresponding to the symmetrical solution (full lines) with $\langle \hat{Q}_{20} \rangle$ ranging from 38 to

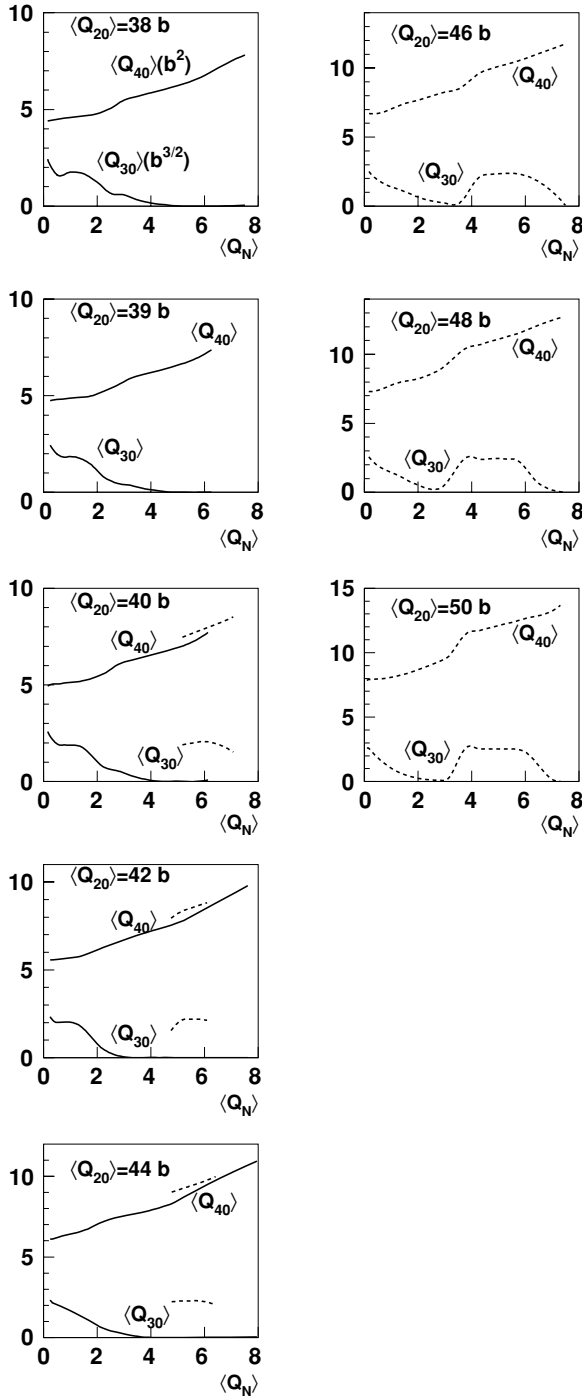


FIG. 10. Variation of the expectation values of the axial octupole and hexadecapole moments along the sections in the $\langle \hat{Q}_N \rangle$ direction at various $\langle \hat{Q}_{20} \rangle$ -values around the exit point. They are expressed in $b^{3/2}$ and b^2 , respectively.

44 b vary smoothly with $\langle \hat{Q}_N \rangle$ as can be seen in Fig. 10. It is remarkable that $\langle \hat{Q}_{40} \rangle$ turns out to vary almost linearly with $\langle \hat{Q}_N \rangle$, which shows that these deformation coordinates may be considered as being redundant. As far as the asymmetrical solution is concerned (dashed lines), the expectation value of \hat{Q}_{30} appears to remain constant and equal to about $2 b^{3/2}$ for $\langle \hat{Q}_N \rangle$ -values around 5 (see Fig. 10). Upon making a cut in

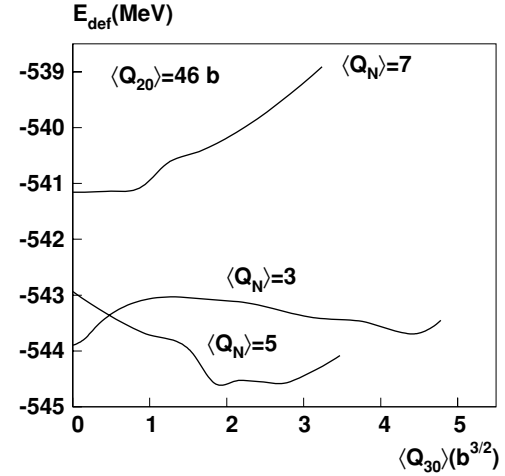


FIG. 11. Sections of the potential energy surface in the $\langle \hat{Q}_{30} \rangle$ direction at three different $\langle \hat{Q}_N \rangle$ -values (3, 5, and 7) and at the same elongation $\langle \hat{Q}_{20} \rangle = 46$ b.

the $\langle \hat{Q}_{30} \rangle$ direction at $\langle \hat{Q}_N \rangle = 5$ with $\langle \hat{Q}_{20} \rangle$ fixed to 46 b for example (see Fig. 11), we have found indeed a minimum at a finite $\langle \hat{Q}_{30} \rangle$ -value of about $2 b^{3/2}$. As one goes away from this $\langle \hat{Q}_N \rangle$ region one gets symmetrical equilibrium solutions (i.e. $\langle Q_{30} \rangle = 0$), which is consistent with the existence of a symmetrical minimum along the sections of Fig. 11 at $\langle \hat{Q}_N \rangle = 3$ as well as $\langle \hat{Q}_N \rangle = 7$. In addition, one may note the appearance of a second minimum at a finite $\langle \hat{Q}_{30} \rangle$ -value of about $4.5 b^{3/2}$ for the cut at $\langle \hat{Q}_N \rangle = 3$ (see Fig. 11). Even though, as already mentioned, $\langle \hat{Q}_{40} \rangle$ varies almost linearly with respect to $\langle \hat{Q}_N \rangle$, it exhibits, however, a kink around the $\langle \hat{Q}_N \rangle$ -value where $\langle \hat{Q}_{30} \rangle$ vanishes (see the right column of Fig. 10).

As an example, a sequence of nuclear shapes is displayed in Fig. 12 showing that, starting from the symmetrical minimum at $\langle \hat{Q}_{20} \rangle = 44$ b—where $\langle \hat{Q}_N \rangle = 4.4$ —the nucleus smoothly acquires a left-right asymmetric deformation yielding the mass asymmetric $^{39}\text{K}+^{31}\text{P}$ fragmentation.

Assuming that the ^{70}Se nucleus adiabatically follows the ascending valley from its ground state up to the exit point, we can consider that the height of the latter relative to the ground state provides an upper limit of the conditional fission barrier height connecting the ground state to the $^{39}\text{K}+^{31}\text{P}$ exit channel. Specifically, we have taken as a saddle point the local maximum at $\langle \hat{Q}_N \rangle \approx 1.6$ along the energy curve computed at $\langle \hat{Q}_{20} \rangle = 44$ b in Fig. 8. It lies 51.5 MeV above the (oblate) ground state. The comparison with experimental data will be presented in the last section after having taken into account the rotational correction as well as the two-body contribution to the center of mass correction.

D. Descending valleys

As discussed in the previous subsection (Sec. III C), a two-body shaped solution corresponding to a $^{39}\text{K}+^{31}\text{P}$ configuration is found at very low $\langle \hat{Q}_N \rangle$ -values (of the order of 0.3) for $\langle \hat{Q}_{20} \rangle = 39$ b and larger elongations. We have

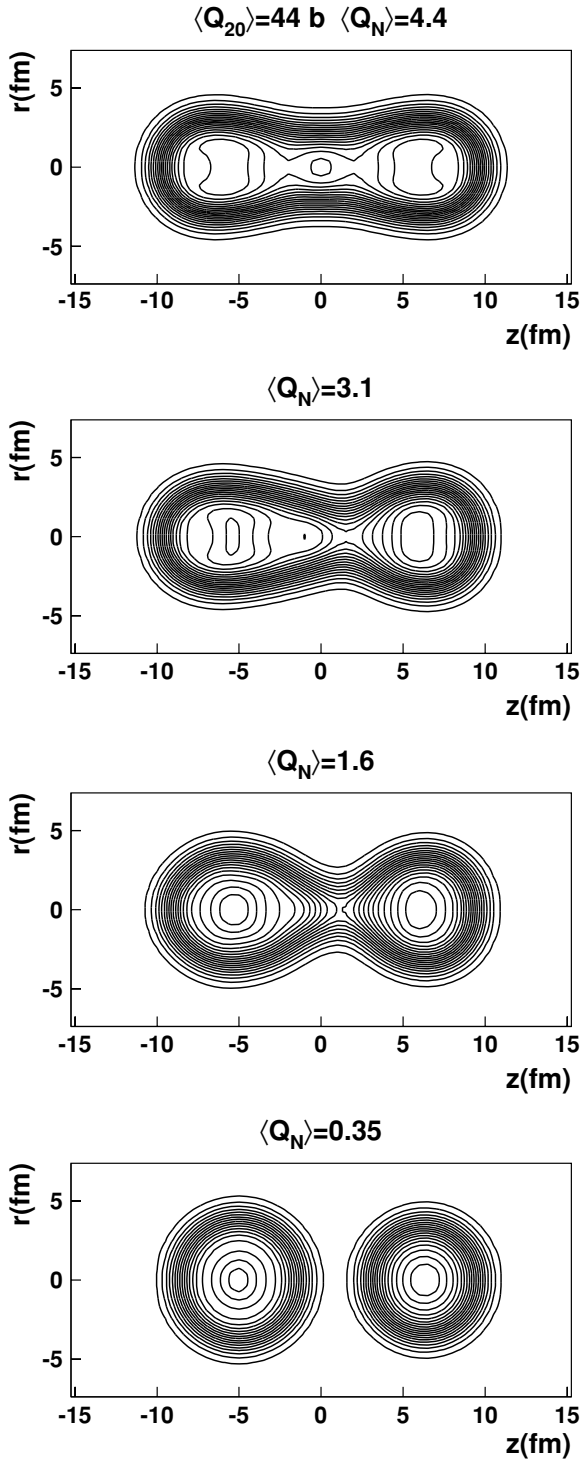


FIG. 12. Sequence of nuclear shapes along the section in the $\langle \hat{Q}_N \rangle$ direction at $\langle \hat{Q}_{20} \rangle = 44$ b starting from the symmetrical one-body solution.

determined the deformation energy curve associated with this fragmentation as a function of $\langle \hat{Q}_{20} \rangle$, in particular the entry point in this valley, that is the lowest $\langle \hat{Q}_{20} \rangle$ -value at which this solution is stable against $\langle \hat{Q}_N \rangle$ deformations. We have thus obtained the dashed curve displayed in Fig. 3 which is reported as a full line in Fig. 13. Along these curves, the energy is a

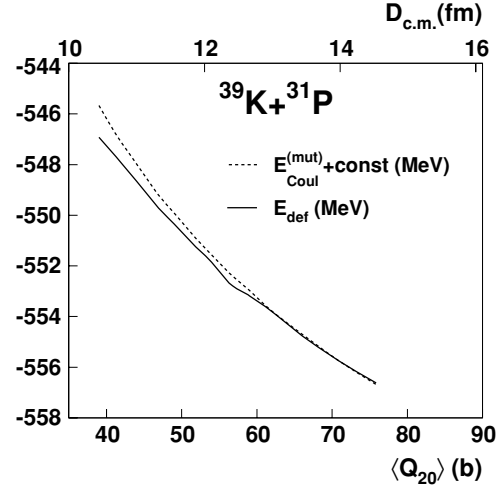


FIG. 13. Deformation energy curve as a function of $\langle \hat{Q}_{20} \rangle$ corresponding to the $^{39}\text{K} + ^{31}\text{P}$ fragmentation (full line). The sum of the mutual Coulomb energy $E_{\text{Coul}}^{(\text{mut})}$ within the approximation of two well-separated spherical fragments Eq. (17) and a fitted constant (see the text) has been displayed as a dotted line.

decreasing function of $\langle \hat{Q}_{20} \rangle$. Asymptotically it should behave like the mutual Coulomb energy $E_{\text{Coul}}^{(\text{mut})}$.

That is why we have also plotted $E_{\text{Coul}}^{(\text{mut})}$ —within an approximation discussed below—to which a constant energy term has been added and fitted so that the so-obtained total energy is as close as possible to the actual deformation energy E_{def} . Since we are only interested, here, in the behavior of E_{def} as a function of $\langle \hat{Q}_{20} \rangle$, we will not discuss the constant term. To calculate the mutual Coulomb energy, we have taken stock on the fact that the two fragments are well separated. Then the expectation value of the axial mass quadrupole moment $\langle \hat{Q}_{20} \rangle$ of the whole fissioning system is related to the intrinsic elongation of the fragments defined with an obvious notation by $\langle \hat{Q}_{20} \rangle^{(i)}$ ($i = 1, 2$), according to the following expression:

$$\langle \hat{Q}_{20} \rangle = \langle \hat{Q}_{20} \rangle^{(1)} + \langle \hat{Q}_{20} \rangle^{(2)} + 2 \frac{A_1 A_2}{A_1 + A_2} D_{c.m.}^2, \quad (15)$$

where $D_{c.m.}$ is the center of mass distance. As can be seen in Fig. 14, the fragment elongations are found to be rapidly decreasing to almost vanishing values. Since they are negligible with respect to $D_{c.m.}^2$, we are thus left with

$$\langle \hat{Q}_{20} \rangle \approx 2 \frac{A_1 A_2}{A_1 + A_2} D_{c.m.}^2. \quad (16)$$

Consequently, for almost spherical fragments, the following expression holds for the mutual Coulomb energy between both fragments:

$$E_{\text{Coul}}^{(\text{mut})} \approx \frac{Z_1 Z_2 e^2}{D_{c.m.}} \approx \sqrt{\frac{2 A_1 A_2}{A_1 + A_2}} \frac{Z_1 Z_2 e^2}{\sqrt{\langle \hat{Q}_{20} \rangle}}. \quad (17)$$

This is the energy—to within a constant term—plotted as a dotted line in Fig. 13. As expected, E_{def} does behave like $E_{\text{Coul}}^{(\text{mut})}$ asymptotically and varies like $\langle \hat{Q}_{20} \rangle^{-1/2}$. Nevertheless, as the elongation nears its value at the entry point of the descending $^{39}\text{K} + ^{31}\text{P}$ valley, the deformation energy curve slightly departs

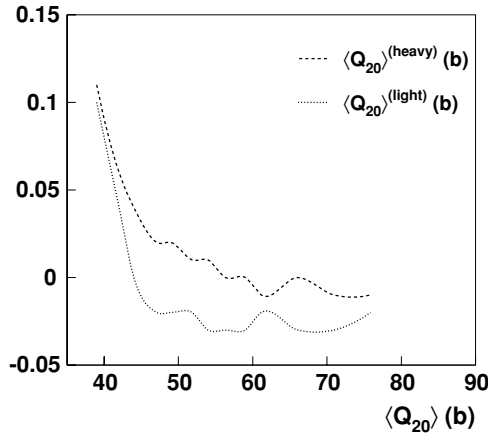


FIG. 14. Expectation values of the mass quadrupole moments of the heavy fragment (dashed line) and the light one (dotted line) expressed in barns as functions of $\langle \hat{Q}_{20} \rangle$ for the $^{39}\text{K}+^{31}\text{P}$ fragmentation.

from the pure Coulombian trend. The above approximation of well-separated fragments becomes therefore less and less valid. Indeed at this elongation, the “tip distance”—measuring the closest distance between the fragments edges, defined at half the saturation density—amounts to 3 fm approximately, so that the nuclear interaction between nucleons in different fragments begins to play a role.

Let us now focus our interest on another characteristic feature of the $^{39}\text{K}+^{31}\text{P}$ fragmentation. The heavy fragment (chosen to be the left one since we consider positive $\langle \hat{Q}_{30} \rangle$ -values) turns out to have a magic neutron number $N = 20$ and an almost magic proton number $Z = 19 \approx 20$, making it very close to the doubly magic ^{40}Ca nucleus. Thus this mass division is clearly driven by shell effects in the heavy fragment. This explains why the fragments are almost spherical (see Fig. 14). We can therefore expect that other fragmentations should be favored by the shell effects in at least one fragment, which should lead to local minima in a section of the potential energy surface, for example, in the $\langle A_{\text{right}} \rangle$ direction (i.e., the expectation value of the nucleon number in the right fragment). That is precisely what we have done upon imposing the elongation at $\langle \hat{Q}_{20} \rangle = 45$ b for instance. We have then obtained the curve displayed in Fig. 15.

Four local minima have been found for the mass of the light fragment, corresponding to different mass divisions of the ^{70}Se nucleus, namely:

- (1) $\langle A_{\text{light}} \rangle = 12$: $^{58}\text{Ni}+^{12}\text{C}$ fragmentation;
- (2) $\langle A_{\text{light}} \rangle = 16$: $^{54}\text{Fe}+^{16}\text{O}$ fragmentation (the corresponding local minimum appears merely as a shoulder at the energy scale of Fig. 15);
- (3) $\langle A_{\text{light}} \rangle = 31$: $^{39}\text{K}+^{31}\text{P}$ fragmentation (see the preceding discussion);
- (4) $\langle A_{\text{light}} \rangle = 35$: $^{35}\text{Cl}+^{35}\text{Cl}$ fragmentation (symmetric fission, associated with a rather shallow minimum).

The three above-mentioned first divisions are clearly driven by shell effects in one of the two fragments. In the first two

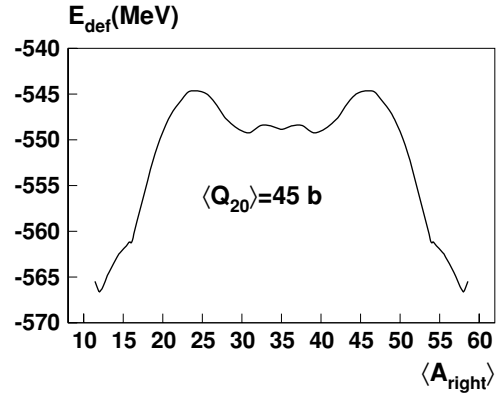


FIG. 15. Section of the potential energy surface at $\langle \hat{Q}_{20} \rangle = 45$ b along the $\langle A_{\text{right}} \rangle$ direction.

cases one fragment is indeed doubly magic or very close to a doubly magic nucleus:

- (1) the ^{58}Ni heavy fragment has a magic proton number $Z = 28$ and almost a magic neutron number $N = 30 \approx 28$;
- (2) the ^{16}O light fragment is doubly magic whereas the heavy one (^{54}Fe) has a magic neutron number $N = 28$;

The case of the $^{39}\text{K}+^{31}\text{P}$ fragmentation has already been discussed. It is interesting to bear in mind that the product of the two fragments charges $\langle Z_{\text{light}} \rangle \langle Z_{\text{heavy}} \rangle$, driving the Coulomb energy scale, decreases with the mass asymmetry. This can explain the increasing energy of the four above-mentioned fragmentations going from $\langle A_{\text{light}} \rangle = 12$ to $\langle A_{\text{light}} \rangle = 35$ at the same $\langle \hat{Q}_{20} \rangle$ -value. It is, indeed, related to the fact that, as already noted, the ^{70}Se has a $x = 0.33$ fissility parameter. It lies therefore slightly below the usually considered Businaro-Gallone point ($x \approx 0.35$). In this mass region, the liquid drop (nonquantum) effects dominate with respect to the shell effects whereas one observes the contrary in the actinides and beyond.

We have studied in particular the energy of the $^{58}\text{Ni}+^{12}\text{C}$ solution as a function of the elongation $\langle \hat{Q}_{20} \rangle$. The corresponding deformation energy curve has been displayed as a dotted line in Fig. 3 and as a full line in the upper panel of Fig. 16. As can be noticed this curve does not follow the expected Coulombian trend—whatever the value of the constant term added to $E_{\text{Coul}}^{(\text{mut})}$. However, when performing the same calculations without any center of mass correction, one obtains the dotted curve in the lower panel of Fig. 16 and a better agreement is found for the lower $\langle \hat{Q}_{20} \rangle$ -values. For larger elongations, the discrepancy between the deformation energy and the Coulombian trend increases with $\langle \hat{Q}_{20} \rangle$.

These two facts might be explained as such. Upon increasing the global elongation and keeping the same number of basis states, one makes the (one center) harmonic oscillator basis less and less suited for the description of two well-separated nuclei. This is seen, for instance, on the larger deformation part of the E_{def} curve in Fig. 16, showing thus a bigger and bigger lack of binding from the expected behavior as the deformation increases. On the other hand, even at the

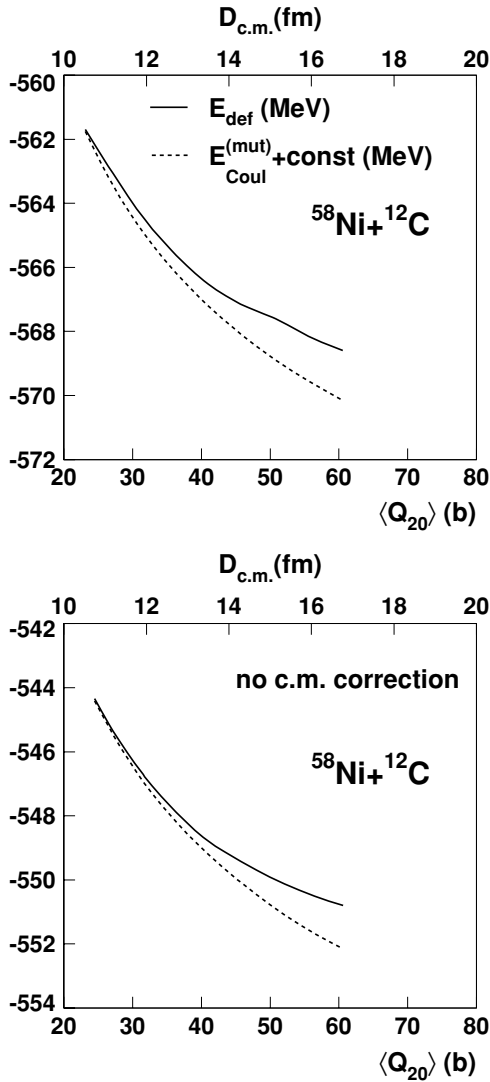


FIG. 16. Deformation energy curve as a function of $\langle \hat{Q}_{20} \rangle$ corresponding to the $^{58}\text{Ni}+^{12}\text{C}$ fragmentation with (upper panel) and without (lower panel) center of mass correction. The sum of the mutual Coulomb energy in the approximation of two well separated spherical fragments Eq. (17) and a fitted constant (see the text for explanation) has been displayed as a dashed line in both cases.

lowest deformations considered in this descending valley, the center of mass correction, tailored for the compound ^{70}Se nucleus, has *a priori* no reasons to be suited to the description of two separated lighter nuclei. This is demonstrated in the lower part of Fig. 16 where a self-consistent model calculation without any center of mass corrections restores the expected $1/r$ behavior of the deformation energy curve before being polluted by the above-mentioned single well basis problem. Since the center of mass correction scales as $1/A$, it is not surprising to find that this effect is more apparent in the $^{58}\text{Ni}+^{12}\text{C}$ case (Fig. 16) than in the $^{39}\text{K}+^{31}\text{P}$ case (Fig. 13). Indeed in the former case a very light nucleus (^{12}C) is involved.

In Sec. III C we have investigated the region of the so-called exit point to define a continuous path from the ground

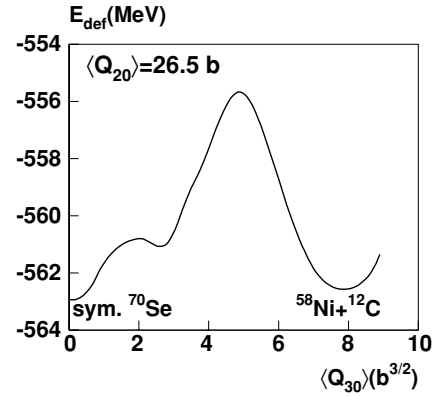


FIG. 17. Section of the potential energy surface at $\langle \hat{Q}_{20} \rangle = 26.5\text{ b}$ along the $\langle \hat{Q}_{30} \rangle$ direction.

state ascending valley to the $^{39}\text{K}+^{31}\text{P}$ descending valley. In order to find an upper limit of the conditional fission barrier height associated with the $^{58}\text{Ni}+^{12}\text{C}$ fragmentation, we have also sought here such a continuous path. For the purpose of this study, we have chosen to make a section in the potential energy surface in the $\langle \hat{Q}_{30} \rangle$ direction, at the elongation for which the solutions belonging to the ascending and descending valleys have equal energies, namely at $\langle \hat{Q}_{20} \rangle = 26.5\text{ b}$. We have then obtained the deformation energy curve plotted in Fig. 17.

As can be seen in Fig. 18, the expectation values of the axial hexadecapole moment $\langle \hat{Q}_{40} \rangle$ and of the neck operator $\langle \hat{Q}_N \rangle$ vary continuously as functions of $\langle \hat{Q}_{30} \rangle$, $\langle \hat{Q}_N \rangle$ experiencing however a rapid decrease around $\langle \hat{Q}_{30} \rangle = 4\text{ b}^{3/2}$ corresponding to the neck rupture.

Thus, the difference between the maximal value of the energy for $\langle \hat{Q}_{30} \rangle = 5\text{ b}^{3/2}$ (see Fig. 17) along this path and the (oblate) ground state energy gives an upper limit for the conditional barrier height between the ground state and the $^{58}\text{Ni}+^{12}\text{C}$ exit channel. It amounts to about 40.9 MeV (before corrections discussed in the next section).

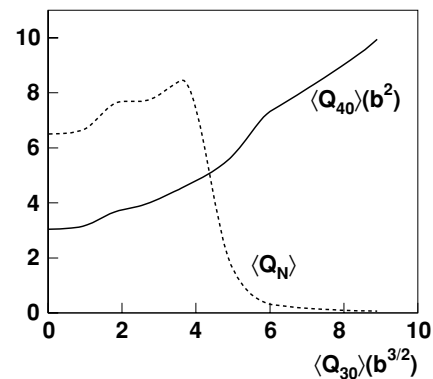


FIG. 18. Variation of $\langle \hat{Q}_{40} \rangle$ (full line) and $\langle \hat{Q}_N \rangle$ (dashed line) along the section of the potential energy surface in the $\langle \hat{Q}_{30} \rangle$ direction displayed in Fig. 17.

IV. ROTATIONAL AND CENTER OF MASS CORRECTIONS, CONDITIONAL BARRIERS

Let us discuss now the approximations made to restore the rotational and translational symmetries broken by our mean field microscopic approach.

As in Ref. [1] the rotation symmetry has been approximately restored in the energy calculation upon applying a correction $\delta E_{\text{rot}} = \langle \mathbf{J}^2 \rangle / 2\mathcal{I}$. There the expectation value of the total angular momentum squared (including the one-body and two-body parts) has been computed for the relevant BCS solution. Correspondingly the moment of inertia \mathcal{I} has been evaluated for the same wave function within the Inglis–Belyaev [35] approximation corrected as in [1] for the self-consistent Thouless–Valatin terms [36]. The effect of such a rotational symmetry restoration on the conditional fission barrier height $B_f(^{58}\text{Ni})$ separating the ground state from the $^{58}\text{Ni}+^{12}\text{C}$ final state is given by the difference between the values of the correction energy δE_{rot} calculated for the maximum along the continuous section of Fig. 17 ($\langle \hat{Q}_{20} \rangle = 26.5$ b), and the (oblate) ground state ($\langle \hat{Q}_{20} \rangle = -2$ b). We have then found, respectively, 6.5 and 2.7 MeV. As noted previously [1] this corrective energy is increasing with $\langle \hat{Q}_{20} \rangle$. From the above values one infers that our corresponding fission barrier may be considered as being overestimated by about 3.8 MeV. As far as the barrier height $B_f(^{39}\text{K})$ separating the ground state from the $^{39}\text{K}+^{31}\text{P}$ exit channel is concerned, the effect of the rotational correction is calculated by the difference of the corresponding δE_{rot} energies at the exit point, where we have obtained $\delta E_{\text{rot}} = 6.8$ MeV, and at the ground state. The corresponding fission barrier is thus lowered by about 4.1 MeV.

The second correction is related to the breaking of the center of mass translational invariance. This has been taken care of as in [1] by correcting its kinetic part, in the variational energy, through a mere subtraction of the one-body part of the center of mass kinetic energy. As thoroughly analyzed in Ref. [37] such an approximation is not free from some ambiguities:

- (1) arbitrariness of throwing away a part of the energy which has to be considered (which, as it appears, partly cancel the one which is retained here);
- (2) source of a systematic error due to a possibly different deformation dependence of the one-body and two-body parts of the energy;
- (3) further ambiguities in deciding whether some or all of the $\hat{\rho}$ -dependence of the $\langle \mathbf{P}^2 \rangle / 2m A$ energy should or should not be considered in the functional derivatives yielding the Hartree–Fock equations [37].

Here, we have limited ourselves to the self-consistent one-body part of the center of mass correction energy. This was motivated, beyond the numerical simplicity arguments, by the fact that the SkM* force parameters have been fitted within this framework. However we have performed some perturbative calculations to yield a qualitative hint of what could be the effect of such a crude approximation on the fission barrier heights. Since the traditional way to treat the center of mass

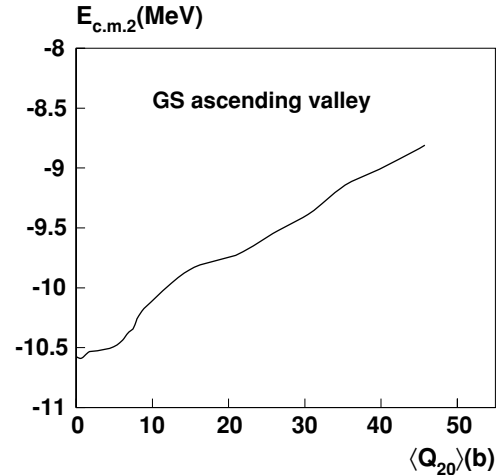


FIG. 19. Two-body contribution to the center of mass kinetic energy along the ground state ascending valley.

correction breaks down when dealing with two well-separated fragments (as above discussed at length in the $^{58}\text{Ni}+^{12}\text{C}$ case), we have restricted ourselves to one-cluster shapes, that is close to the ground state ascending valley. The top of the two considered mass-asymmetric fission barriers corresponds to such a shape, before the neck rupture (corresponding to a value of $\langle \hat{Q}_N \rangle$ of about 2 for the upper descending valley and about 3 for the lower one). We can thus have a reasonable confidence in the above-mentioned perturbative calculations of the two-body contribution to the center of mass correction around the exit point and the saddle point of the $^{58}\text{Ni}+^{12}\text{C}$ exit channel.

As can be seen in Fig. 19 showing the variation of the two-body part $E_{c.m.2}$ of the center of mass kinetic energy as a function of $\langle \hat{Q}_{20} \rangle$ along the ascending valley, $E_{c.m.2}$ slightly increases along this valley. It is found to decrease the height of the exit point relatively to the ground state by about 2.7 MeV and to lower the saddle point along the path down to the $^{58}\text{Ni}+^{12}\text{C}$ exit channel by 2.4 MeV.

As a result, taking the rotational and two-body center of mass corrections into account, the conditional fission barrier heights which we finally obtain amount to $B_f(^{58}\text{Ni}) = 34.7$ MeV and $B_f(^{39}\text{K}) = 44.9$ MeV.

These values can now be compared with the available experimental data, obtained by Fan and collaborators [5]. More precisely we have considered the mass-asymmetric fission barriers B_Z extracted from “individual” fittings of the excitation functions with a transition state formalism and appearing in Table IV of Ref. [5]. Our fission barrier height for the $^{58}\text{Ni}+^{12}\text{C}$ exit channel should be compared with $B_6 = 25.28$ MeV, whose overall uncertainty is estimated to amount to 3%, that is 0.8 MeV. Our $B_f(^{58}\text{Ni})$ -value overestimates therefore the experimental value by about 9.4 MeV. In the case of the $^{39}\text{K}+^{31}\text{P}$ fragmentation, the experimental value $B_{15} = 35.09$ MeV—with the same relative uncertainty—is about 9.8 MeV lower than our $B_f(^{39}\text{K})$ -value. Some other conditional barriers have also been deduced in Ref. [5] as resulting from a global fit (i.e., a fit involving most of the studied fragmentations). These global values turn out to be

very close to those given by the individual fitting procedure, but since they were not reported in the $^{58}\text{Ni}+^{12}\text{C}$ case, we have not considered them here.

The discrepancies between our barrier values and the data correspond roughly to an overestimation of about 1/3. It is however interesting to note that the difference between B_{15} and B_6 , namely $B_{15} - B_6 = 9.8$ MeV, is quite well reproduced since our calculations give correspondingly $B_f(^{39}\text{K}) - B_f(^{58}\text{Ni}) = 10.2$ MeV. Furthermore, to put the above-mentioned overestimation in the proper perspective, one should first bear in mind that we have only given here upper limits for the fission barrier heights. It is also worth recalling that it was before this work commonly thought that our results should vastly overestimate the experimental barrier heights on the basis of a semiclassical estimate of the curvature liquid drop energy based on the leptodermous approximation for the density [4]. It is hard to disentangle, in such an appraisal, the deficiencies of the effective force parametrizations and the limits of the density modelization. Our results might rather indicate that the leptodermous approximation could be not really adapted for nuclei as light as ^{70}Se . An additional reason for this might be, as we have seen, that the scission points for such a light compound nucleus are very close to the saddle points. Indeed, one deals here with fission barriers corresponding to somewhat well-marked neck formations, which are clearly not expected to be well represented within the leptodermous expansion.

To close this section, it is worth mentioning the theoretical work of two groups of authors, namely Royer and Zbiri using the generalized liquid drop model on the one hand [6], Möller, Sierk, and Iwamoto using the macroscopic-microscopic model on the other hand [7]. These authors have reported calculations of conditional macroscopic fission barrier heights of ^{70}Se (only in the symmetric case for the second group). In both approaches the microscopic correction (including shell and pairing effects) remains of course to be properly added. In order to compare their experimental B_Z -values with the two above sets of calculated barrier heights, the authors of Ref. [5] have therefore subtracted to B_Z the microscopic correction calculated in the ground state of ^{70}Se by Möller *et al.* [38]. The resulting values (quoted as “exp.”) are displayed in Table I together with the barrier heights calculated by Royer *et al.* [6] and Möller *et al.* [7]. In principle, the macroscopic fission barrier height B_Z^{macro} should be calculated by subtracting the microscopic correction at the saddle point on the fission path leading to a given Z -value for the charge of the light fragment. The macroscopic barrier height B_Z^{macro} indeed

TABLE I. Conditional macroscopic fission barriers for the ^{70}Se nucleus extracted from experimental data [5] (after correction for microscopic effects) and calculated within two different approaches by Royer *et al.* [6] and Möller *et al.* [7].

Z_{light}	Exp.	Royer <i>et al.</i>	Möller <i>et al.</i>
6	29.5	34.5	–
15	39.3	40.5	–
17	39.4	40.6	37.6

writes, in the notations of Ref. [38]:

$$B_Z^{\text{macro}} = B_Z + E_{s+p}^{(\text{GS})} - E_{s+p}^{(\text{sadd.Z})}, \quad (18)$$

where $E_{s+p}^{(\epsilon)}$ is the shell-plus-pairing correction evaluated for the microscopic solution corresponding to the deformation noted here generically by ϵ . In the experimental reference [5] the energy $E_{s+p}^{(\text{sadd.Z})}$ has been neglected. This produces a systematic error in the resulting B_Z^{macro} -values. In the absence of any definite calculations of these shell and pairing effects in the macroscopic-microscopic approach of Refs. [6,7] at the saddle points, we can at best formulate the conjecture that the systematic error of the so-called “experimental values” is of the order of a couple of MeV.

V. CONCLUSIONS AND PERSPECTIVES

Conditional fission barrier heights of the ^{70}Se nucleus, which lies below the Businaro–Gallone point, have been calculated in the microscopic Hartree–Fock–BCS approach (using the SkM* parametrization of the Skyrme effective force and a seniority force for the pairing residual interaction) in the cases of two asymmetric divisions: $^{58}\text{Ni}+^{12}\text{C}$ and $^{39}\text{K}+^{31}\text{P}$. They have appeared to be locally stable due to shell effects in at least one of the fragments. The obtained fission barriers overestimate the available data by about 10 MeV. This result however may be deemed as an encouraging one in two accounts. Indeed the barrier heights were expected much higher since some studies based on approximations of mean field semiclassical approaches—including some using the SkM* Skyrme force—have lead to a much too high curvature-energy value a_c as compared to the value obtained from fits of experimental fission barrier heights and ground state masses. Moreover, one should be reminded that our calculated barrier heights are upper limits since the whole deformation space has not been systematically explored. In this respect, the present study has also underlined the complexity of the potential energy surface of light nuclei, due to the proximity of the scission point from the saddle point, contrarily to the situation prevailing in actinide or heavier nuclei. A more appropriate description of this surface implies a global scanning of the deformation space built up with a relevant number of well-chosen deformation coordinates. The correct localization of physical saddle points can then be done, e.g., by implementing a water immersion method as the one used in five dimensions by Möller (see for example Ref. [7] for a description of the method and Refs. [12–14] quoted therein) and recently extended to surfaces of any dimension by one of us (L.B.) in collaboration with Möller.

ACKNOWLEDGMENTS

We are grateful to A. J. Sierk for pointing out to us the interest of calculating fission barriers for such light nuclei and for many interesting comments. We would like to acknowledge also valuable discussions with P. Möller and D. Samsøen on various subjects ranging from a general understanding of nuclear fission to some calculational aspects. One of the

authors (Ph.Q.) thanks the Theoretical Division at LANL for the excellent working conditions extended to him during

numerous visits. This research was supported by the U.S. Department of Energy under Contract No. W-7405-ENG-36.

-
- [1] L. Bonneau, P. Quentin, and D. Samsøen, *Eur. Phys. J. A* **21**, 391 (2004).
- [2] S. Cohen and W. J. Swiatecki, *Ann. Phys. (NY)* **22**, 406 (1963).
- [3] R. Vandenbosch and J. R. Huizenga, in *Nuclear Fission* (Academic Press, New York, 1973), p. 17.
- [4] W. Stocker, J. Bartel, J. R. Nix, and A. J. Sierk, *Nucl. Phys.* **A489**, 252 (1988).
- [5] T. S. Fan, K. X. Jing, L. Phair, K. Tso, M. McMahan, K. Hanold, G. J. Wozniak, and L. G. Moretto, *Nucl. Phys.* **A679**, 121 (2000).
- [6] G. Royer and K. Zbiri, *Nucl. Phys.* **A697**, 630 (2002).
- [7] P. Möller, A. J. Sierk, and A. Iwamoto, *Phys. Rev. Lett.* **92**, 072501 (2004).
- [8] J. Bartel, P. Quentin, M. Brack, C. Guet, and H.-B. Håkansson, *Nucl. Phys.* **A386**, 79 (1982).
- [9] L. Próchniak, P. Quentin, D. Samsøen, and J. Libert, *Nucl. Phys.* **A730**, 59 (2004).
- [10] R. W. Hasse and W. D. Myers, *Geometrical Relationships of Macroscopic Nuclear Physics* (Springer-Verlag, Berlin, 1988), Chap. 6.
- [11] J.-F. Berger, J. D. Anderson, P. Bonche, and M. S. Weiss, *Phys. Rev. C* **41**, 2483(R) (1990).
- [12] S. Bjornholm and W. J. Swiatecki, *Nucl. Phys.* **A391**, 471 (1982).
- [13] S. Cwiok, V. V. Pashkevich, J. Dudek, and W. Nazarewicz, *Nucl. Phys.* **A410**, 254 (1983).
- [14] S. Cwiok, Z. Lojewski, and V. V. Pashkevich, *Nucl. Phys.* **A444**, 1 (1985).
- [15] G. D. Adeev and V. V. Pashkevich, *Nucl. Phys.* **A502**, 405c (1989).
- [16] A. Y. Rusanov, V. V. Pashkevich, and M. G. Itkis, *Phys. At. Nucl.* **62**, 547 (1999).
- [17] P. Möller and J. R. Nix, *Nucl. Phys.* **A229**, 269 (1974).
- [18] P. Möller, J. R. Nix, and W. J. Swiatecki, *Nucl. Phys.* **A469**, 1 (1987).
- [19] P. Möller, J. R. Nix, and W. J. Swiatecki, *Nucl. Phys.* **A492**, 349 (1989).
- [20] J.-F. Berger, M. Girod, and D. Gogny, *Nucl. Phys.* **A428**, 23c (1984).
- [21] J.-F. Berger, M. Girod, and D. Gogny, *Nucl. Phys.* **A502**, 85c (1989).
- [22] J. L. Egido, L. M. Robledo, and R. R. Chasman, *Phys. Lett.* **B393**, 13 (1997).
- [23] M. Warda, J. L. Egido, L. M. Robledo, and K. Pomorski, *Phys. Rev. C* **66**, 014310 (2002).
- [24] H. Goutte, P. Casoli, and J.-F. Berger, *Nucl. Phys.* **A734**, 217 (2004).
- [25] H. Goutte, J.-F. Berger, P. Casoli, and D. Gogny, *Phys. Rev. C* **71**, 024316 (2005).
- [26] W. John, E. K. Hulet, R. W. Lougheed, and J. J. Wesolowski, *Phys. Rev. Lett.* **27**, 45 (1971).
- [27] K. F. Flynn *et al.*, *Phys. Rev. C* **5**, 1725 (1972).
- [28] D. C. Hoffman, J. B. Wilhelmy, J. Weber, W. R. Daniels, E. K. Hulet, R. W. Lougheed, J. H. Landrum, J. F. Wild, and R. J. Dupzyk, *Phys. Rev. C* **21**, 972 (1980).
- [29] E. K. Hulet *et al.*, *Phys. Rev. Lett.* **56**, 313 (1986).
- [30] P. Möller, D. G. Madland, A. J. Sierk, and A. Iwamoto, *Nature (London)* **409**, 785 (2001).
- [31] J.-F. Berger and M. Girod (private communication).
- [32] P. Sarriguren, E. Moya de Guerra, and A. Escuderos, *Nucl. Phys.* **A658**, 13 (1999).
- [33] A. Petrovici, K. W. Schmid, and A. Faessler, *Nucl. Phys.* **A728**, 396 (2003).
- [34] A. Ahmed *et al.*, *Phys. Rev. C* **24**, 1486 (1981).
- [35] S. D. Belyaev, *Nucl. Phys.* **24**, 322 (1961), and references quoted therein.
- [36] D. J. Thouless and J. G. Valatin, *Nucl. Phys.* **31**, 211 (1962).
- [37] M. Bender, K. Rutz, P.-G. Reinhard, and J. A. Maruhn, *Eur. Phys. J. A* **7**, 467 (2000).
- [38] P. Möller, J. R. Nix, W. D. Myers, and W. J. Swiatecki, *At. Data Nucl. Data Tables* **59**, 185 (1995).